The Astrophysical Journal Supplement Series, 261:35 (10pp), 2022 August https://doi.org/10.3847/1538-4365/ac7f9b
© 2022. The Author(s). Published by the American Astronomical Society.
OPEN ACCESS

Wavelengths and Energy Levels of Singly Ionized Nickel (Ni II) Measured Using Fourier Transform Spectroscopy

Christian P. Clear[1], Juliet C. Pickering[1], Gillian Nave[2], Peter Uylings[3], and Ton Raassen[3,4]
[1] Blackett Laboratory, Imperial College London, London, SW7 2AZ, UK; christian.clear@imperial.ac.uk
[2] National Institute of Standards and Technology, Gaithersburg, MD, 20889-8422, USA
[3] Anton Pannekoek Institute for Astronomy, University of Amsterdam, Science Park 904, 1098 XH Amsterdam, The Netherlands
[4] SRON Netherlands Institute for Space Research, Sorbonnelaan 2, 3584 CA Utrecht, The Netherlands
Received 2022 June 1; revised 2022 July 5; accepted 2022 July 5; published 2022 August 4

Abstract

High-resolution spectra of singly ionized nickel (Ni II) have been recorded using Fourier transform spectroscopy in the region 143–5555 nm (1800–70,000 cm^{-1}) with continuous, nickel–helium hollow cathode discharge sources. An extensive analysis of identified Ni II lines resulted in the confirmation and revision of 283 previously reported energy levels, from the ground state up to the $3d^8(^ML)6s$ subconfigurations. Typical energy-level uncertainties are a few thousandths of a cm^{-1}, representing at least an order-of-magnitude reduction in uncertainty with respect to previous measurements. Twenty-five new energy levels have now been established and are reported here for the first time. Eigenvector compositions of the energy levels have been calculated using the orthogonal operator method. In total, 159 even and 149 odd energy levels and 1424 classified line wavelengths of Ni II are reported and will enable more accurate and reliable analyses of Ni II in astrophysical spectra.

Unified Astronomy Thesaurus concepts: Laboratory astrophysics (2004); Atomic spectroscopy (2099); Line positions (2085); Spectral line identification (2073); Spectroscopy (1558); Spectral line lists (2082); Atomic data benchmarking (2064); Stellar atmospheric opacity (1585); Stellar spectral lines (1630)

Supporting material: machine-readable tables

1. Introduction

High-accuracy, high-resolution atomic data are vital for the interpretation of modern astrophysical spectra. However, for many elements, the existing laboratory-measured atomic data are either of insufficient accuracy or are incomplete, and much potential information is lost when identifying, calculating and modeling astrophysical parameters. Transition wavelengths and energy-level values are of particular importance for calculating elemental abundances in stellar atmospheres, which require both realistic atmospheric models and a complete and accurate atomic database. The development of three-dimensional nonlocal thermodynamic equilibrium hydrodynamical atmospheric models has greatly improved modeling capability, however the underpinning atomic database has not seen equivalent improvement for many atomic species. For astrophysical spectra, wavelengths are also essential in determining the components of blended spectral features. As most lines in stellar spectra are blended, accurate wavelengths from experimental spectra or calculated Ritz wavelengths from experimentally determined energy levels are essential to disentangle these blends.

A major focus of the Imperial College and National Institute of Standards and Technology (NIST) atomic spectroscopy groups are the astrophysically important iron-group elements. The complex energy-level structures of this group, with partially filled 3*d* shells, allow for many possible electronic transitions and, as a result, iron-group elements produce thousands of spectral lines compared to hundreds for lighter, less complex elements. Combined with their rich spectra, iron-group elements also have relatively high abundances, dominating the solar spectrum and accounting for the majority of opacity observed in stars.

A significant proportion of iron-group element analyses date back over 50 years and are often based solely on lower-resolution grating spectroscopy. These data are no longer sufficient for the interpretation of modern astrophysical spectra and high-accuracy atomic measurements are urgently needed. To address this issue, there has recently been a concerted effort to update the atomic database with high-resolution Fourier transform (FT) measurements (Thorne et al. 2013; Nave & Johansson 2013; Sansonetti & Nave 2014; Liggins et al. 2021), but work still remains for many elements and ionization stages (Pickering et al. 2020) including singly ionized nickel.

Within the iron group, nickel has the second greatest solar abundance (Scott et al. 2015) and has been identified in the spectra of many astrophysical sources, including supernovae (Dhawan et al. 2018), evolved stars (Richardson et al. 2011), globular clusters (Kirby et al. 2018), planetary nebulae (Delgado Inglada et al. 2016), and quasi-stellar objects (Boisse & Bergeron 2019).

1.1. Previous Measurements of Ni II

The first major analysis of Ni II was carried out by Shenstone (1970, 1971) who measured 4300 lines between 10,000 cm^{-1} and 137,500 cm^{-1} (72.5–1000 nm) using grating spectroscopy of a nickel–helium hollow cathode lamp (HCL). The large number of measured Ni II lines enabled Shenstone to derive an extensive energy-level system of 320 even and 336 odd measured energy levels. The low configurations, $3d^9$, $3d^8(^ML)4s$, and $3d^7(^ML)4s^2$, were nearly complete and Shenstone observed series in $3d^8(^ML)ns$, *np*, *nd*, *nf*, and *ng*, up to 9*s* for the $3d^8(^3F)$ parent

Original content from this work may be used under the terms of the Creative Commons Attribution 4.0 licence. Any further distribution of this work must maintain attribution to the author(s) and the title of the work, journal citation and DOI.

term and 6*s* for the $3d^8(^1D)$, (^3P), and (^1G) parent terms. All levels found by Shenstone were designated using the L–S coupling scheme.

Analysis of the Ni II spectrum was extended into the infrared (IR) using FT spectrometry by Brault & Litzén (1983). They recorded the spectra of a nickel–helium HCL over the range 2000–10,000 cm^{-1} (1000–5000 nm) and identified two groups of Ni II lines. The first were transitions between the previously identified energy levels $3d^8(^3F)5f$–$3d^8(^3F)6g$ and the second group were $3d^8(^3F)5g$–$3d^8(^3F)6h$ transitions, which led to the establishment of the $(^3F)6h$ energy levels.

The most recent compilation of Ni II energy levels is that of Sugar & Corliss (1985) (referred to as S+C from here on). The majority of the Ni II energy levels in the compilation are from Shenstone, with the addition of Brault and Litzén's 6*g* and 6*h* levels. Based on the conclusion of Brault and Litzén that the high-lying levels of Ni II are well described by *jK* coupling, S+C redesignated Shenstone's levels for all configurations with $l \geqslant 3$ according to the *jK* coupling scheme. As Shenstone's work did not include level uncertainties, S+C estimated these to be ± 0.05 cm^{-1}. Brault and Litzén also estimated their level uncertainties to be ± 0.05 cm^{-1}, as they were limited by the accuracy of Shenstone's $3d^8(^3F)5f$ and $3d^8(^3F)5g$ levels.

In this work, we address the current need for high-accuracy atomic data by providing new and improved wavelengths and energy-level values for the lower-lying levels of Ni II (from the ground state up to the $3d^8(^ML)6s$ subconfigurations) as the result of an extensive term analysis of high-resolution FT spectra.

2. Experimental Details

2.1. Fourier Transform Spectra

The analysis in this work incorporates data from nine new spectra recorded on two instruments and two additional archival spectra. The vacuum ultraviolet (VUV) FT spectrometer (FTS) at Imperial College (IC-FTS) (Thorne et al. 1987) was used to record six spectra in the region 15,798–75,000 cm^{-1} (133–633 nm). The 2 m FTS at NIST (NIST-FTS) produced two further spectra covering the region 9000–23,000 cm^{-1} (435–1111 nm). In addition, two FT spectra recorded in the 1980s at the Kitt Peak National Observatory (KPNO) by J. Brault, extracted from the National Solar Observatory archives (NSO 2021), were analyzed to extend the spectral range of this work into the region 1550–9900 cm^{-1} (1010–6450 nm).

The six IC-FTS spectra were measured using a water-cooled HCL source (Holmes 2015). Helium was chosen as the carrier gas, as nickel–helium spectra gave an enhancement of signal-to-noise ratio (S/N) for Ni II lines, compared to spectra recorded using neon and argon (Clear 2018). The HCL emitted lines of Ni I and Ni II as well as neutral and singly ionized species of the helium carrier gas, and in one spectrum (NiHeCH) a small number of impurities (O I and N I), most likely due to a small leak in the HCL. The cathode was a high-purity (99.99+%, natural isotope composition), open-ended nickel cylinder, 40 mm long with an internal diameter of 8 mm. The anode was formed by the metal casing of the lamp. The optimum operating pressure and current for the Imperial College lamp was determined to be 1000 mA and 10 mbar helium. To enable wavenumber calibration with argon standards, an additional spectrum in the visible region (NiArDH) was recorded using argon as the carrier gas.

The two spectra recorded by the NIST-FTS used a Ni–He water-cooled HCL, based on the design of Danzmann et al. (1988). The NIST HCL used a high-purity (99.99+%, natural isotope composition) nickel cylinder 60 mm in length with an internal diameter of 8 mm as the cathode. The optimum operating conditions were determined to be 2000 mA with a helium pressure of 5.3 mbar. The operating conditions for the HCL used for the two KPNO spectra (NiHeAH and NiHeBH) are recorded as "4 Torr at 280 mA" and "6.3 Torr at 1000 mA" respectively (NSO 2021). No details regarding the dimensions or purity of the HCL cathode are provided in the NSO archives.

A summary of the experimental parameters of the spectra used in this study is given in Table 1. Column 1 is the shorthand spectrum name detailing the element (Ni), HCL carrier gas (He), spectrum order (spectra were labeled in ascending order from the IR with labels A to H) and current (H for high current). NiHeBC is the exception to this naming scheme as it was a later addition to the analysis, needed to bridge the calibration between NiHeBH and NiHeCH. Column 2 gives the date of measurement and the serial number of the spectrum. Column 3 is the wavenumber range of the spectrum used in the final linelist. Columns 4–7 give the measurement FTS, beam-splitter material, filter, and detector, respectively. Column 8 is the resolution of the spectrum in cm^{-1}. Columns 9 and 10 give the current and carrier gas pressure of the HCL. Column 11 is the wavenumber calibration correction factor and associated calibration uncertainty for the spectrum (discussed in Section 2.2).

To enable intensity calibration of the Ni–He spectra, additional spectra of radiometrically calibrated standard lamps were recorded immediately before and after each nickel spectrum. The HCL and standard lamp were set up in a "T" configuration perpendicular to the FTS input aperture and an aluminum-coated mirror used to select between the two lamps. The spectrum NiHeDH, recorded at Imperial College, used a tungsten standard lamp calibrated by the National Physical Laboratory, UK. The spectra recorded at NIST (NiHeBC and NiHeCH) used a tungsten lamp, calibrated by Optronics Laboratories Inc, FL, USA, with a sapphire window to enable observations further into the IR. The spectra recorded at Imperial College in the visible to UV range (NiHeEH to NiHeHH) used a deuterium standard lamp, with a magnesium fluoride window, calibrated by the Physikalisch-Technische Bundesanstalt, Germany.

The FTS instrument response function was calculated by comparison of the standard lamp spectra with their calibrated radiances. Intensities of successive spectra were placed on a consistent, relative scale using overlapping nickel lines. The relative intensities given in the linelist of this work should only be regarded as a rough guide and are not suitable for calculating branching fractions. The KPNO spectra do not have associated standard lamp spectra and are therefore not intensity calibrated.

2.2. Wavenumber Calibration

Line lists of observed lines in each of the measured spectra were produced using the analysis program XGREMLIN (Nave et al. 2015). Voigt profiles were least-squares fitted to spectral lines to determine their wavenumber, FWHM, peak S/N, and integrated intensity. For a small number of lines which exhibited an asymmetric profile, generally with low S/Ns, wavenumbers were determined by a center-of-gravity (COG) fit.

Table 1
Experimental Parameters for Spectra Used in This Work

Spectrum	Date/ Serial Number	Range[a] (cm^{-1})	FTS	Beam Splitter	Filter	Detector	Res. (cm^{-1})	Curr. (A)	Press. (mbar)	k_{eff}[b] (10^{-7})
NiHeAH	1983/01/06 .002	1832–5076	KPNO 1 m	CaF_2	Wedged GE	InSb	0.011	0.28	5.3	5.37 ± 1.23
NiHeBH	1980/03/20 .001	5076–9032	KPNO 1 m	CaF_2	ISP2 + SI	InSb	0.012	1.0	8.4	-2.84 ± 0.46
NiHeBC	2017/04/20 .001	9032–9970	NIST 2 m	SiO_2	...	InSb	0.020	2.0	5.3	6.03 ± 0.18
NiHeCH	2017/04/20 .004	9970–19,284	NIST 2 m	SiO_2	10SWF-1000B	Si diode	0.020	2.0	5.3	6.31 ± 0.15
NiHeDH	2016/10/25 .010.029	19,284–25,767	IC VUV	MgF_2	GG385	R11568	0.037	1.0	10.0	-2.81 ± 0.11
NiHeEH	2016/11/08 .010.031	25,767–35,720	IC VUV	MgF_2	UG5c	R11568	0.045	1.0	10.0	-6.27 ± 0.18
NiHeFH	2016/10/20 .050.078	35,720–51,193	IC VUV	MgF_2	...	R7154	0.050	1.0	10.0	-4.51 ± 0.23
NiHeGH	2016/11/16 .031.061	51,193–59,128	IC VUV	MgF_2	170 nm	R8486	0.060	1.0	10.0	-7.55 ± 0.28
NiHeHH	2016/11/17 .020.051	59,128–68,735	IC VUV	MgF_2	...	R1259	0.070	1.0	10.0	-6.97 ± 0.41
NiArDH	2016/11/18 .010.025		IC VUV	MgF_2	GG385	R11568	0.037	1.0	10.0	-6.16 ± 0.03

Notes.
[a] Denotes the range of the spectrum used in the final linelist.
[b] k_{eff} is the wavenumber calibration factor for the spectrum and associated calibration uncertainty.

Nickel ($Z = 28$) has five stable isotopes: ^{58}Ni (68%), ^{60}Ni (26%), ^{61}Ni (1%), ^{62}Ni (3%), and ^{64}Ni (1%) (Berglund & Wieser 2011) and exhibits strong isotope shift (IS) in lines involving levels in the doubly excited system, particularly in transitions involving the $3d^8(^M L)4p - 3d^7\,4s^2$ configurations. For transitions within the singly excited system of Ni II, to which all of the energy levels in this work belong, no IS was observed and they were therefore assumed to be much lower than the Doppler widths of the individual isotopic lines. Thus IS is negligible for all transitions observed in this work and it did not lead to asymmetric line profiles. As the two dominant Ni isotopes have nuclear spin quantum numbers $I = 0$, there is also no hyperfine splitting present.

The wavenumbers of all lines in the individual spectra were wavenumber calibrated using 26 Ar II reference lines (Learner & Thorne 1988; Nave & Sansonetti 2004) between 19,429–23,644 cm^{-1} (422.9–514.7 nm). First, the nickel spectrum measured using an argon carrier gas (NiArDH) was calibrated to the Ar II standard wavenumbers of Whaling et al. (1995). Following the calibration of NiArDH, the wavenumber calibration was transferred to the Ni–He spectrum in the visible (NiHeDH) via Ni I lines present in both spectra. Calibration was then extended to the IR and VUV by nickel lines in the overlapping regions of successive spectra. Only strong nickel lines which had been fitted using Voigt profiles were used for the calibration.

The statistical uncertainty, $\delta\sigma_{stat}$, in the measurement of the wavenumber of a line fitted with a Voigt profile is given by Sansonetti & Nave (2014):

$$\delta\sigma_{stat} = \frac{[R \times (\mathrm{FWHM})]^{\frac{1}{2}}}{(\mathrm{S/N})} \quad (1)$$

where R is the resolution of the spectrum in cm^{-1} and the FWHM has units of $10^{-3}\,cm^{-1}$. To avoid unreasonably low uncertainties for strong lines, the S/N was limited to a maximum of 100 during calculation of the statistical uncertainty. For lines fitted with a COG fit, the statistical uncertainty was doubled.

The wavenumber scale of an FTS is linear and so wavenumber calibration is performed by multiplication of observed wavenumbers by a scale factor, with the calibrated wavenumber, σ_{corr}, given by:

$$\sigma_{corr} = (1 + k_{eff})\sigma_{obs} \quad (2)$$

where σ_{obs} is the observed wavenumber and k_{eff} is the calibration correction factor of the spectrum. k_{eff} is calculated as the weighted average of the individual correction factors, k_i, of each observed line matched to a reference line:

$$k_{eff} = \frac{\Sigma_i(k_i w_i)}{\Sigma_i w_i} \quad (3)$$

where

$$k_i = \frac{\sigma_{ref,i}}{\sigma_{obs,i}} - 1 \quad (4)$$

and $\sigma_{ref,i}$ and $\sigma_{obs,i}$ are the wavenumbers of the reference and observed lines, respectively. The weighting used in the average, w_i, is equal to the reciprocal of the square of the individual correction factor uncertainty, δk_i, which is the addition in quadrature of the relative statistical uncertainty of $\sigma_{obs,i}$ and the relative total uncertainty of $\sigma_{ref,i}$:

$$\delta k_i = \left[\left(\frac{\delta\sigma_{obs,stat,i}}{\sigma_{obs,i}}\right)^2 + \left(\frac{\delta\sigma_{ref,total,i}}{\sigma_{ref,i}}\right)^2\right]^{\frac{1}{2}}. \quad (5)$$

The uncertainty in the calibration correction factor of each spectrum, known as the calibration uncertainty δk_{eff}, is calculated from the individual line correction factors and their weightings:

$$\delta k_{eff} = \frac{[\Sigma_i(w_i + w_i^2(k_{eff} - k_i)^2)]^{\frac{1}{2}}}{\Sigma_i w_i} \quad (6)$$

as given by Haris & Kramida (2017), adapted from Radziemski & Andrew (1965).

To ensure that calibration uncertainty increases with wavenumber separation from the Ar II standards, the δk_{eff} for each spectrum was added to the δk_{eff} of the previous spectrum after calibration. The individual k_{eff} and their uncertainties for each spectrum are given in Table 1. A detailed treatment of the calibration process used in this work is given by Haris & Kramida (2017), with specific details for the calibration of the spectra used in this work given in Clear (2018).

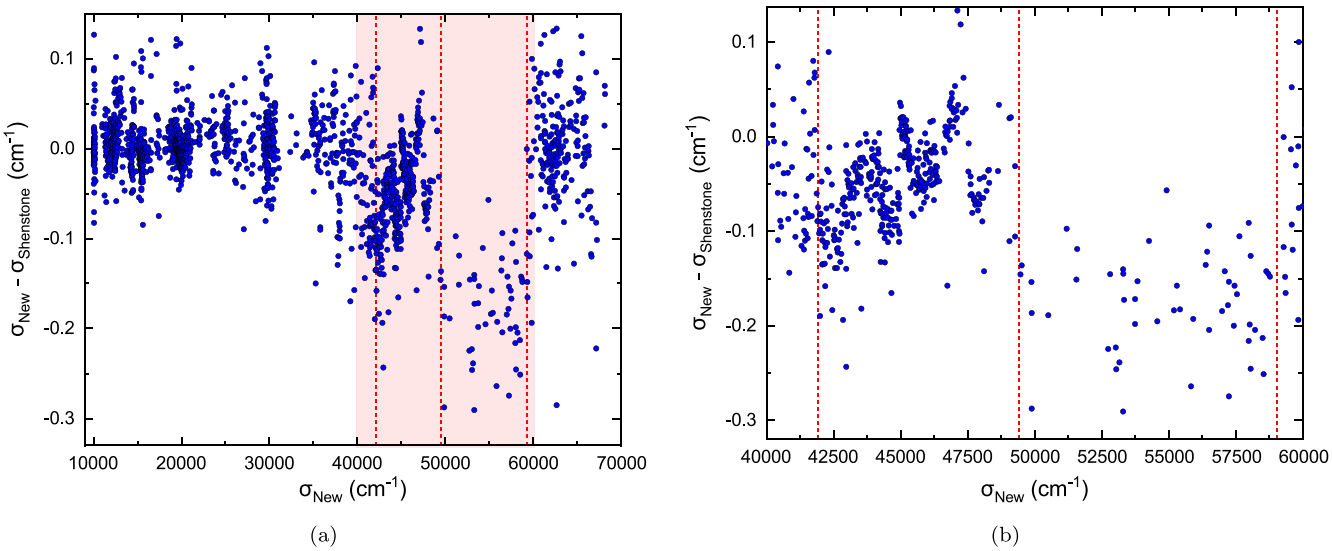

Figure 1. Comparison of Ni II FT wavenumbers in this work with the grating wavenumbers of Shenstone (1970). (a) Full wavenumber range of Shenstone (1970). (b) Expanded region of (a) (highlighted with the red background) from 40,000–60,000 cm^{-1}. Red dotted lines on both plots indicate the approximate spectral regions covered by the two problematic photographic plates recorded by Shenstone.

The total wavenumber uncertainty of a line, $\delta\sigma_{\rm tot}$ (in cm^{-1}), is then the sum in quadrature of the statistical uncertainty of the line and the relative calibration uncertainty of its spectrum multiplied by the line's calibrated wavenumber:

$$\delta\sigma_{\rm tot} = [\delta\sigma_{\rm stat}^2 + (\delta k_{\rm eff} \times \sigma_{\rm corr})^2]^{\frac{1}{2}}. \quad (7)$$

The total uncertainty of symmetric, strong lines (S/N > 100) varies from ∼0.0008 cm^{-1} in the IR to ∼0.002 cm^{-1} in the VUV. The weakest lines in the spectra have an S/N of approximately 3 and uncertainties that vary from ∼0.007 cm^{-1} in the IR to ∼0.04 cm^{-1} in the VUV.

The uncertainty of the original Ar II standard lines is common to all observed lines and so becomes weighted out of the energy-level value and Ritz wavenumber uncertainties during the level optimization procedure. To account for this, the uncertainty of the Ar II standard lines (1×10^{-8} times the wavenumber) was added to the uncertainties of the optimized energy-level values and Ritz wavenumbers. A global calibration uncertainty, based on the calibration uncertainty of NiHeHH, which contains the important Ni II resonance lines, was set at four parts in 10^8 and was used as the minimum uncertainty for all optimized energy-level values and calculated Ritz wavenumbers.

The wavenumber range of each spectrum in our final calibrated linelist is given in Table 1. These ranges were determined by assessing the uncertainties of lines appearing in the overlapping regions of successive spectra. Our final linelist contains 6681 spectral lines from nine spectra across the range 1832–68,735 cm^{-1} (145–5458 nm).

2.3. Comparison with Published Wavenumbers

The wavenumber differences between the calibrated Ni II lines reported in this work and those of Shenstone (1970, 1971), $\sigma_{\rm new} - \sigma_{\rm Shenstone}$, are shown in Figure 1. The calibration of the two line lists agrees well in the regions 10,000–40,000 cm^{-1} and 60,000–70,000 cm^{-1}, with wavenumber differences distributed approximately evenly about $\Delta\sigma = 0$.

However, for two regions, 40,000–50,000 cm^{-1} and 50,000–60,000 cm^{-1}, there are significant deviations, with $\Delta\sigma \approx 0.05\ cm^{-1}$ and $\Delta\sigma \approx 0.17\ nm^{-1}$ respectively. Issues in the calibration of lines measured in our work were eliminated as a cause of these shifts by comparison of Ni I wavenumbers observed in our spectra with values reported by Litzén et al. (1993), which showed no systematic shifts between measured lines (Clear 2018).

The problematic regions are most likely two separate grating plates measured by Shenstone. The region 40,000–50000 cm^{-1} also displays a nonlinearity in the $\Delta\sigma$ dispersion, indicating a further problem with linear wavelength correction of the plates in this region. A potential source of the shifts could be spectrometer issues reported by Shenstone in his 1970 paper in which he describes a "close satellite" in one of the spectrometers he used.

Regardless of the source, the error in wavelength calibration had a direct effect on the energy levels in Shenstone's work which have transitions in these two regions. Most importantly, the 50,000–60,000 cm^{-1} region contains many of the critical $3d^9 - 3d^8(^3F)4p$ resonance lines, which tie the entire energy-level system to the ground state. As a result, all energy levels reported in Shenstone (1970) and Sugar & Corliss (1985) were shifted by ∼0.17 cm^{-1} relative to the ground state.

3. Ni II Spectral Analysis

3.1. Line Identification

Ni I lines in the calibrated linelist were identified from Ritz wavenumbers calculated using FT-determined levels published by Litzén et al. (1993). The carrier gas lines, He I and He II, and impurity lines (O I and N I) were identified by comparison with compilations of data in the NIST Atomic Spectra Database (Kramida et al. 2021). In total, 1318 Ni I, 25 He II, 117 He I, and 131 impurity lines were identified using the sources outlined above, leaving 5090 unclassified lines in our linelist.

Ni II lines were initially identified by comparison with Ritz wavenumbers calculated from energy levels previously reported by S+C. Due to the wavenumber shift in Shenstone's resonance lines, discussed above, all S+C levels (excluding the $3d^9$ ground state configuration) were shifted by $-0.17\ cm^{-1}$ before calculating Ritz wavenumbers.

3.2. Ni II Spectrum

A total of 1424 lines observed in this work have been classified as Ni II transitions between the energy levels included in this paper and are given in Table 2. Only lines for transitions between level values revised or newly discovered using our FTS observations in this paper are given. The first column shows the logarithm of the relative integrated line intensity. As discussed in Section 2.2, lines in the IR, with wavenumbers $< 9032\,\mathrm{cm}^{-1}$, were not intensity calibrated. Column 2 gives the S/N. A guide to line width in the form of the FWHM is given in the third column, in units of $0.001\,\mathrm{cm}^{-1}$. The observed wavenumber, Ritz wavenumber, and their uncertainties are given in columns 4–7. Air and vacuum Ritz wavelengths and their uncertainty are shown in columns 8–10. Air wavelengths are given for all lines between 200 nm and 2 μm, following the five-parameter dispersion formula of Peck & Reeder (1972). The upper and lower levels of the transition are given in columns 11 and 12 in the form: configuration, term, and J value. Columns 13 and 14 show the upper and lower energy-level values. The final column notes any blends or irregularities with the line.

4. The Atomic Structure of Ni II

Nickel belongs to the ($3d$) iron group of elements, and has the ground level $3d^9\ ^2D_{\frac{5}{2}}$. The nd and $(n+1)s$ electrons of the iron-group elements have very similar binding energies, especially for singly ionized elements, and there is competition for electron filling order between these configurations. As a result, there is some overlap between the three lowest configurations of Ni II: $3d^9$, $3d^84s$ and $3d^84s^2$. Configuration interaction between these overlapping configurations makes observation of, nominally, two-electron transitions possible.

The energy-level structure of Ni II is therefore described by two configuration systems, with the excited electronic configurations split into the singly excited (normal) and doubly excited systems. Figure 2 shows a schematic diagram of the singly excited term system of Ni II which is built on a core of electrons, described by a single term. The singly excited system is built on the $3d^8(^ML)$ parent terms of Ni III and the doubly excited system is built on the $3d^7(^ML)$ grandparent terms of Ni IV. For singly ionized members of the iron group, the singly excited system tends to dominate, with fewer transitions observed within the doubly excited system. In Ni II, the strongest transitions are between the $3d^84s$ and $3d^84p$ and the $3d^84p$ and $3d^84d$ configurations of the same parent term, resulting in a spectrum rich in UV lines.

Strong transitions to energy levels of the doubly exited system lie in the VUV, beyond the lower-wavelength spectral range of an FTS, requiring grating spectroscopy to measure. Grating data have been recorded at NIST and the analysis of the spectra and the energy levels of the doubly excited system will be the subject of a future paper.

5. Calculations of Energy Levels and Level Eigenvector Composition

To correctly identify energy levels and assign level designations, accurate calculations of eigenvector compositions, predicted level energies and transition probabilities are crucial. In complex systems such as the iron-group metals, with their many closely lying energy levels, a semiempirical approach to calculation, in which parameters of a model Hamiltonian are adjusted to yield eigenvalues as closely as possible to the experimental energies, is most appropriate to achieve accurate results.

The calculations used in this work to predict energy-level values and eigenvector compositions were achieved with the orthogonal operator method. This method is an extension and refinement of Racah's classical parametric approach as incorporated in Cowan's programs (Cowan 1981). As the parameters in the orthogonal operator set are as independent as possible, the fits are highly stabilized, which allows the introduction of a variety of physical effects, ranging from dominant to subtle, one after another.

In this way, small interactions, such as higher-order perturbational or pure relativistic effects, can be accounted for. As a result, the mean deviation of the fit is frequently reduced by an order of magnitude in a physically significant way. A detailed explanation of the orthogonal operator approach is found in Uylings & Raassen (2019) and Uylings (2021).

Although the orthogonal operator method is semiempirical in character, ab initio calculations (Froese Fischer et al. 2016; Jönsson et al. 2017) do constitute an important part of the procedure, especially to predict fine-structure effects relativistically. Even without varying its additional parameters, the orthogonal operator method still provides an improved description of complex spectra. See the FERRUM project (Hartman et al. 2015) and the analysis of $5d$ spectra (Azarov 2018) for recent use.

In most cases the magnetic effects within one particular configuration are dominant. However, configuration interaction cannot be neglected. Therefore the even-parity model space is extended to seven configurations: $3d^9 + 3d^84s + 3d^74s^2 + 3d^84d + 3d^85s + 3d^85d + 3d^86s$. The five-configuration odd-parity basis contains $3d^84p + 3d^74s4p + 3d^64s^24p + 3d^85p + 3d^84f$. The overall mean deviations are $33\,\mathrm{cm}^{-1}$ for the even system and $82\,\mathrm{cm}^{-1}$ for the odd system. In more detail, the mean deviation is $7.8\,\mathrm{cm}^{-1}$ for the lowest three even configurations and $15\,\mathrm{cm}^{-1}$ for $3d^84p$.

In all cases, the main source of error remains an inaccurate description of the mixing between different levels within a single configuration, not the limited number of interacting configurations. In a forthcoming article, the complete list of transition probabilities calculated by the orthogonal operator method with accurate intermediate coupling will be detailed and these intensities will be compared with the experimental FTS values for identified lines.

6. Energy-level Optimization

Identified Ni II lines were used to derive optimized energy levels using the computer program LOPT (Kramida 2011), which employs a weighted least-squares fitting routine to calculate energy-level values and their uncertainties. Line weightings were set as the inverse squares of their total wavenumber uncertainties (Equation (7)). Multiply identified lines were assigned a low weighting (i.e., a high uncertainty) to ensure that they did not contribute to the level optimization, but retained their parameters to aid line identification and to derive Ritz wavelengths and uncertainties.

The level optimization was performed in several stages, beginning with the strong resonance lines of the $3d^9 - 3d^8(^ML)4p$ transitions, which anchor the energy-level system to the ground state. Newly optimized energy levels were then used to improve the identification of further lines in the

Table 2
Classified Lines of Ni II

Int.	S/N	FWHM (10^{-3} cm^{-1})	σ_{obs} (cm^{-1})	Unc. (cm^{-1})	σ_{Ritz} (cm^{-1})	Unc. (cm^{-1})	λ_{air} (nm)	λ_{vac} (nm)	Unc. (nm)	Configuration		E_L (cm^{-1})	E_U (cm^{-1})	Notes
										Lower Level	Upper Level			
5.77	9	22	2127.6835	0.0018	2127.6970	0.0008	⋯	46,999.173	0.017	$3d^8(^3F)5p\ ^2D_{\frac{3}{2}}$	$3d^8(^3P)5s\ ^2P_{\frac{3}{2}}$	107,141.921	109,269.618	N
5.15	5	22	2222.933	0.003	2222.9361	0.0009	⋯	44,985.549	0.018	$3d^8(^1D)5d\ ^2F_{\frac{7}{2}}$	$3d^8(^3P_1)4f\ [3]_{\frac{5}{2}}$	133,734.788	135,957.724	
4.87	5	23	2587.431	0.006	2587.4311	0.0019	⋯	38,648.37	0.03	$3d^8(^1D)5p\ ^2P_{\frac{1}{2}}$	$3d^8(^3F)5d\ ^4D_{\frac{3}{2}}$	118,443.322	121,030.753	
6.91	16	42	2936.4801	0.0015	2936.4804	0.0006	⋯	34,054.374	0.007	$3d^8(^3F)4d\ ^4H_{\frac{7}{2}}$	$3d^8(^3F)5p\ ^2G_{\frac{9}{2}}$	101,144.435	104,080.915	
5.31	6	20	3478.5798	0.0024	3478.5792	0.0008	⋯	28,747.369	0.007	$3d^8(^3F)4d\ ^2D_{\frac{3}{2}}$	$3d^8(^3F)5p\ ^2D_{\frac{3}{2}}$	103,663.342	107,141.921	
5.05	6	19	4056.656	0.003	4056.6565	0.0007	⋯	24,650.843	0.004	$3d^8(^3F)4d\ ^2D_{\frac{5}{2}}$	$3d^8(^3F)5p\ ^2F_{\frac{5}{2}}$	103,025.385	107,082.042	
6.39	24	20	4069.9457	0.0009	4069.9466	0.0004	⋯	24,570.3471	0.0023	$3d^8(^3F)6s\ ^4F_{\frac{9}{2}}$	$3d^8(^3P)5p\ ^4D_{\frac{7}{2}}$	116,833.052	120,902.999	
3.98	3	17	4313.847	0.005	4313.8473	0.0006	⋯	23,181.163	0.003	$3d^8(^3F)6s\ ^2F_{\frac{7}{2}}$	$3d^8(^3P)5p\ ^2D_{\frac{5}{2}}$	117,074.569	121,388.417	
7.03	38	28	4855.4347	0.0012	4855.4304	0.0004	⋯	20,595.4964	0.0018	$3d^8(^3F)4d\ ^2G_{\frac{9}{2}}$	$3d^8(^3F)5p\ ^4F_{\frac{9}{2}}$	99,442.661	104,298.092	B
6.33	8	43	4880.304	0.003	4880.3040	0.0005	⋯	20,490.5267	0.0022	$3d^8(^3F)4d\ ^2G_{\frac{7}{2}}$	$3d^8(^3F)5p\ ^2G_{\frac{7}{2}}$	101,740.073	106,620.377	
7.24	23	39	4926.2955	0.0012	4926.2920	0.0004	⋯	20,299.2435	0.0018	$3d^8(^3F)4d\ ^4F_{\frac{9}{2}}$	$3d^8(^3F)5p\ ^2G_{\frac{9}{2}}$	99,154.623	104,080.915	N
7.60	12	106	4943.888	0.003	4943.8891	0.0005	⋯	20,226.9909	0.0022	$3d^8(^3F)4d\ ^4D_{\frac{5}{2}}$	$3d^8(^3F)5p\ ^4D_{\frac{5}{2}}$	99,559.165	104,503.054	
5.68	13	21	4969.6167	0.0025	4969.6139	0.0006	⋯	20,122.2876	0.0023	$3d^8(^3F)4d\ ^4G_{\frac{9}{2}}$	$3d^8(^3F)5p\ ^4G_{\frac{9}{2}}$	100,619.096	105,588.710	N
6.40	16	24	5014.6146	0.0013	5014.6157	0.0005	19,936.2651	19,941.7076	0.0019	$3d^8(^3F)4d\ ^4G_{\frac{11}{2}}$	$3d^8(^3F)5p\ ^4G_{\frac{11}{2}}$	99,132.589	104,147.205	
6.96	15	45	5032.4291	0.0017	5032.4293	0.0009	19,865.696	19,871.119	0.004	$3d^8(^1D)6s\ ^2D_{\frac{5}{2}}$	$3d^8(^3P_1)4f\ [3]_{\frac{5}{2}}$	130,925.295	135,957.724	
5.96	15	24	5075.8338	0.0023	5075.8327	0.0006	19,695.8239	19,701.2009	0.0021	$3d^8(^3F)4d\ ^4F_{\frac{7}{2}}$	$3d^8(^3F)5p\ ^4F_{\frac{5}{2}}$	100,592.788	105,668.621	

Note. The columns are as follows: (1) the $\log_{10}$ of the relative intensity of the line. (2) S/N of the line. (3) FWHM of the line in units of 0.001 cm^{-1}. (4)–(5) The observed wavenumber of the line in cm^{-1} and it is uncertainty. (6)–(7) The Ritz wavenumber of the line, derived from the optimization of energy levels and its uncertainty. (8) The Ritz vacuum wavelength of the line. (9) The Ritz air wavelength of the line. Air wavelengths are calculated using the five-parameter dispersion formula of Peck & Reeder (1972). (10) The uncertainty in Ritz wavelength. (11) The configuration, term, and J value of the lower energy level. (12) The configuration, term, and J value of the upper energy level. (13)–(14) Lower and upper energy-level values respectively, in units of cm^{-1}. (15) Notes about the observed line: (N) line observed in an area of strong noise and/or ringing, (B) blended line/asymmetric line profile.

(This table is available in its entirety in machine-readable form.)

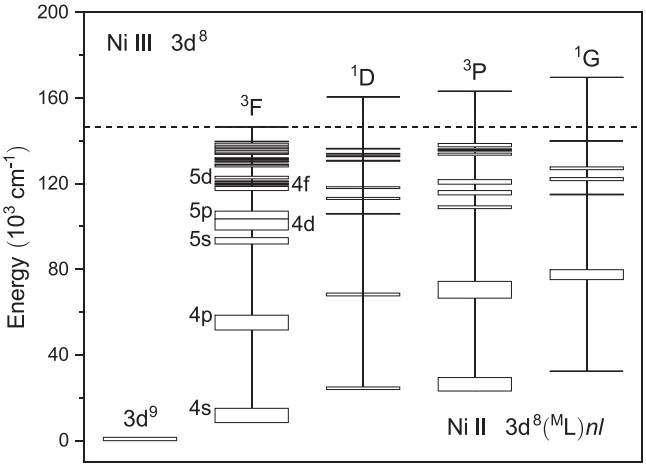

Figure 2. The singly excited (normal) system $3d^8(^M L)nl$ of Ni II. The upper region of the diagram, above the dotted line indicating the ionization energy of Ni II, displays the (^{M}L) parent terms of the 3d^8 configuration of Ni III against level energy. Vertical lines connect each of the parent terms to boxes representing Ni II levels in their daughter subconfigurations. The height of the boxes indicate the maximum energy range of the levels in each subconfiguration. The terms of the 3d^9 configuration are also shown.

observed spectrum. The optimization was repeated many times, at each stage adding in lines for transitions to further levels. Lines that exhibited large residuals in the fitting were examined to determine if they should be omitted from the fit, due to blends or asymmetries, or have their initial identification discarded or revised. The process was repeated until no further levels could be optimized. Finally, a search for new energy levels using unclassified lines in our linelist was performed, with the aid of our new calculations.

The energy levels resulting from this term analysis are provided in Table 3. The first three columns include the configuration, term and J value of the level. The level energy and uncertainty are given in columns 4 and 5. Energy-level uncertainties range from 0.0011–0.0018 cm^{-1} for well-defined levels. The number of observed lines that determined the level fit is given in column 6. The eigenvector component(s) and their calculated percentage contributions to the energy level are shown in columns 7–14. The final column provides any notes about the level, e.g a newly discovered level or a level redesignated from S+C.

6.1. Revision of Previously Known Energy Levels

A total of 283 of the 292 energy-level values published by S+C (up to and including the $3d^8(^M L)6s$ configurations) have been revised following our term analysis. The remaining nine levels could not be confirmed using lines in our FTS spectra. Of these nine, five levels are from the $3d^8(^3P)5d$ configuration. The strongest transitions to these levels are predicted to lie further into the VUV than the wavenumber limit of the IC-FTS. Future work with grating spectra may be able to provide wavelengths for these transitions and enable the values of these levels to be revised.

The configuration, term, or J value of 38 levels have also been revised from their original designation in S+C. Our calculations of eigenvector compositions were key to determining where these changes were necessary. The revised designations are summarized in Table 4.

The differences between our new energy-level values and those in S+C are shown in Figure 3. The error bars show level uncertainties in this work and the ∼0.05 cm^{-1} uncertainty of S+C. The systematic shift between our revised energy levels and those published by S+C has been discussed in Section 2.3.

6.2. New Energy Levels

Following the revision of previously known energy levels, unclassified lines in our spectra and predicted energy values from our calculations were used to search for new energy-level values. The wavenumbers of unclassified lines were added to or subtracted from our revised energy-level values and the results searched for groups of transitions that lay within a given tolerance of each other (typically 0.05 cm^{-1}), possibly indicating previously unknown levels. Our calculated transition probabilities and observed relative intensities were then used as a guide to identify the energy levels based on their transitions. In total, 25 new energy levels have been identified in this work and optimized, and are highlighted with "n" in Table 3.

6.2.1. New Levels of the 3d^8(^{3}F)nl Subconfigurations

Two new (^3F)5d level values have been found, with several new IR transitions securing these. In total, 14 newly classified lines have been assigned to transitions from the (^3F)5d levels. All levels of the (^3F)5d subconfiguration have now been found, but one level, the (^3F)5d ^{2}P$_{\frac{1}{2}}$ found by Shenstone, could not be verified in this work due to weak transitions in the FTS spectral range.

The ($^3F_3$)4f and ($^3F_2$)4f subconfigurations are also now complete with the discovery of two new levels, both [1]$_{\frac{1}{2}}$. Both levels were secured with good S/N lines to (^3F)4d levels, resulting in 10 newly classified lines. The ($^3F_4$)4f subconfiguration is almost complete, with only ($^3F_4$)4f [1]$_{\frac{3}{2}}$ found by Shenstone remaining unrevised due to the transitions involved being too weak in our FTS spectra.

6.2.2. New Levels of the 3d^8(^{1}D)nl Subconfigurations

The four new levels of the $3d^8(^1D)nl$ subconfigurations, 5p ^{2}P$_{\frac{1}{2}}$, 6s ^{2}D$_{\frac{3}{2}}$, 6s ^{2}D$_{\frac{1}{2}}$, and ($^1D_2$)4f [3]$_{\frac{5}{2}}$, had previously been assigned to different level energies by Shenstone. These levels were not supported by transitions in our work, but four new level energies which fitted excellently with predicted energy-level values and involving line intensities that matched well with our calculated transition probabilities were found and verified. The levels for the (^1D)nl subconfigurations up to 6s are now complete, except for (^1D)5d $^2S_{\frac{1}{2}}$ which Shenstone was unable to find either, due to a lack of sufficiently strong transitions. The four new levels resulted in the classification of 29 Ni II lines.

6.2.3. New Levels of the 3d^8(^{3}P)nl Subconfigurations

The new levels for the (^3P)nl subconfigurations comprise the majority of the newly discovered levels in this work. Ten of the new levels mean that the (^3P)5p, (^3P)4d, ($^3P_1$)4f, and ($^3P_0$)4f subconfigurations are now fully complete, with all levels known. The other four new levels are from the (^3P)5d subconfiguration, but five levels of this subconfiguration were unable to be found or revised, due to a lack of strong lines in our FTS spectra. The addition of grating spectral lines

Table 3
Energy Levels of Ni II

Energy Level			Energy	Unc.	No. of	Eigenvector Components									Notes
Configuration	Term	J	(cm^{-1})	(cm^{-1})	Lines										
$3d^9$	^{2}D	$\frac{5}{2}$	0.0000	0.0000	13	100%	$3d^9\ ^2$D								
$3d^9$	^{2}D	$\frac{3}{2}$	1506.9621	0.0016	9	100%	$3d^9\ ^2$D								
$3d^8(^3F)4s$	^{4}F	$\frac{9}{2}$	8393.8741	0.0014	9	100%	$3d^8(^3F)4s\ ^4$F								
$3d^8(^3F)4s$	^{4}F	$\frac{7}{2}$	9330.0014	0.0013	12	98%	$3d^8(^3F)4s\ ^4$F	2%	$3d^8(^3F)4s\ ^2$F						
$3d^8(^3F)4s$	^{4}F	$\frac{5}{2}$	10115.5875	0.0013	13	99%	$3d^8(^3F)4s\ ^4$F	1%	$3d^8(^3F)4s\ ^2$F						
$3d^8(^3F)4s$	^{4}F	$\frac{3}{2}$	10663.8120	0.0014	7	99%	$3d^8(^3F)4s\ ^4$F	1%	$3d^8(^1D)4s\ ^2$D						
$3d^8(^3F)4s$	^{2}F	$\frac{7}{2}$	13550.2968	0.0013	17	98%	$3d^8(^3F)4s\ ^2$F	2%	$3d^8(^3F)4s\ ^4$F						
$3d^8(^3F)4s$	^{2}F	$\frac{5}{2}$	14995.5023	0.0013	15	98%	$3d^8(^3F)4s\ ^2$F	1%	$3d^8(^1D)4s\ ^2$D	1%	$3d^8(^3F)4s\ ^4$F				
$3d^8(^3P)4s$	^{4}P	$\frac{5}{2}$	23108.1243	0.0014	17	57%	$3d^8(^3P)4s\ ^4$P	42%	$3d^8(^1D)4s\ ^2$D						
$3d^8(^1D)4s$	^{2}D	$\frac{3}{2}$	23796.0234	0.0014	15	71%	$3d^8(^1D)4s\ ^2$D	26%	$3d^8(^3P)4s\ ^4$P	3%	$3d^8(^3P)4s\ ^2$P				
$3d^8(^3P)5d$	^{4}F	$\frac{9}{2}$	136518.993	0.005	3	84%	$3d^8(^3P)5d\ ^4$F	16%	$3d^8(^1D)5d\ ^2$G						
$3d^8(^3P)5d$	^{4}F	$\frac{7}{2}$	136588.997	0.005	4	60%	$3d^8(^3P)5d\ ^4$F	26%	$3d^8(^3P)5d\ ^2$F	11%	$3d^8(^1D)5d\ ^2$G	2%	$3d^8(^3P)5d\ ^4$D		
$3d^8(^3P)5d$	^{2}D	$\frac{5}{2}$	136667.474	0.005	3	42%	$3d^8(^3P)5d\ ^2$D	23%	$3d^8(^3P)5d\ ^4$F	13%	$3d^8(^3P)5d\ ^4$P	11%	$3d^8(^3P)5d\ ^2$F	n	
$3d^8(^3P)5d$	^{4}P	$\frac{1}{2}$	136725.399	0.005	4	82%	$3d^8(^3P)5d\ ^4$P	12%	$3d^8(^1D)5d\ ^{2S}$	3%	$3d^8(^3P)5d\ ^4$D	2%	$3d^8(^3P)5d\ ^2$P		
$3d^8(^3P)5d$	^{2}F	$\frac{7}{2}$	136796.145	0.005	4	62%	$3d^8(^3P)5d\ ^2$F	29%	$3d^8(^3P)5d\ ^4$F	6%	$3d^8(^3P)5d\ ^4$D	2%	$3d^8(^1D)5d\ ^2$G	n	
$3d^8(^3P)5d$	^{4}F	$\frac{5}{2}$	136960.448	0.005	4	63%	$3d^8(^3P)5d\ ^4$F	20%	$3d^8(^3P)5d\ ^2$D	9%	$3d^8(^3P)5d\ ^4$D	6%	$3d^8(^3P)5d\ ^4$P		
$3d^8(^3P)5d$	^{2}P	$\frac{1}{2}$	137049.852	0.005	3	87%	$3d^8(^3P)5d\ ^2$P	6%	$3d^8(^1D)5d\ ^2$P	3%	$3d^8(^3P)5d\ ^4$D	2%	$3d^8(^1D)5d\ ^{2S}$	n	
$3d^8(^3P)5d$	^{4}P	$\frac{5}{2}$	137070.114	0.005	4	57%	$3d^8(^3P)5d\ ^4$P	30%	$3d^8(^3P)5d\ ^2$F	6%	$3d^8(^3P)5d\ ^2$D	4%	$3d^8(^3P)5d\ ^4$F	n	
$3d^8(^3P)5d$	^{2}P	$\frac{3}{2}$	137211.689	0.005	5	54%	$3d^8(^3P)5d\ ^2$P	39%	$3d^8(^3P)5d\ ^2$D	4%	$3d^8(^3P)5d\ ^4$F	2%	$3d^8(^3P)5d\ ^4$D		
$3d^8(^1G)6s$	^{2}G	$\frac{9}{2}$	140005.977	0.006	3	100%	$3d^8(^1G)6s\ ^2$G								

Note. The columns are as follows: (1)–(3) The energy-level label consisting of: (1) configuration, (2) term, and (3) J value. (4) Energy-level value in cm^{-1}. (5) Energy-level uncertainty in cm^{-1} (6) The number of lines contributing to the level fit. (7)–(14) Eigenvector components and percentage contribution to the level. (15) Notes about the level: (r) indicates the level label has been changed from the designation in Sugar & Corliss (1985) and (n) indicates a new level.

(This table is available in its entirety in machine-readable form.)

Table 4
Ni II Energy-level Label Redesignations

Energy[a] (cm^{-1})	Previous Label (Sugar & Corliss 1985)	New Label (This Work)
100,389.331	$3d^8(^3F)4d\ ^4F_{\frac{5}{2}}$	$3d^8(^3F)4d\ ^4F_{\frac{5}{2}}$
100,475.637	$3d^8(^3F)4d\ ^4G_{\frac{7}{2}}$	$3d^8(^3F)4d\ ^4G_{\frac{7}{2}}$
100,619.096	$3d^8(^3F)4d\ ^4G_{\frac{9}{2}}$	$3d^8(^3F)4d\ ^4G_{\frac{9}{2}}$
104,646.382	$3d^8(^3F)5p\ ^4F_{\frac{7}{2}}$	$3d^8(^3F)5p\ ^4F_{\frac{7}{2}}$
116,191.242	$3d^8(^3P)4d\ ^4F_{\frac{5}{2}}$	$3d^8(^3P)4d\ ^2D_{\frac{5}{2}}$
117,074.569	$3d^8(^3F)6s\ ^4F_{\frac{7}{2}}$	$3d^8(^3F)6s\ ^2F_{\frac{7}{2}}$
117,763.693	$3d^8(^1D)5p\ ^2_{\frac{3}{2}}$	$3d^8(^1D)5p\ ^2D_{\frac{3}{2}}$
118,293.986	$3d^8(^3F)6s\ ^2F_{\frac{7}{2}}$	$3d^8(^3F)6s\ ^4F_{\frac{7}{2}}$
118,442.516	$3d^8(^1D)5p\ ^2_{\frac{3}{2}}$	$3d^8(^1D)5p\ ^2P_{\frac{3}{2}}$
120,143.993	$3d^8(^3F)5d\ ^2_{\frac{5}{2}}$	$3d^8(^3F)5d\ ^2D_{\frac{5}{2}}$
120,189.314	$3d^8(^3F_3)4f\ [1]_{\frac{1}{2}}$	$3d^8(^3F_3)4f\ [0]_{\frac{1}{2}}$
120,198.983	$3d^8(^3F_3)4f\ [1]_{\frac{3}{2}}$	$3d^8(^3F_3)4f\ [2]_{\frac{3}{2}}$
120,222.672	$3d^8(^3F_3)4f\ [2]_{\frac{3}{2}}$	$3d^8(^3F_3)4f\ [1]_{\frac{3}{2}}$
121,042.313	$3d^8(^3P)5p\ ^2_{\frac{3}{2}}$	$3d^8(^3P)5p\ ^4D_{\frac{3}{2}}$
121,050.372	$3d^8(^3P)5p\ ^2D_{\frac{5}{2}}$	$3d^8(^3P)5p\ ^4D_{\frac{5}{2}}$
121,090.532	$3d^8(^3F_2)4f\ [1]_{\frac{1}{2}}$	$3d^8(^3F_2)4f\ [1]_{\frac{3}{2}}$
121,115.421	$3d^8(^3F)5d\ ^4D_{\frac{3}{2}}$	$3d^8(^3F)5d\ ^4P_{\frac{3}{2}}$
121,178.343	$3d^8(^3F_2)4f\ [4]_{\frac{7}{2}}$	$3d^8(^3F_2)4f\ [3]_{\frac{7}{2}}$
121,192.101	$3d^8(^3F_2)4f\ [3]_{\frac{7}{2}}$	$3d^8(^3F_2)4f\ [4]_{\frac{7}{2}}$
121,227.604	$3d^8(^3F)5d\ ^2_{\frac{5}{2}}$	$3d^8(^3F)5d\ ^4F_{\frac{5}{2}}$
121,240.722	$3d^8(^3F)5d\ ^4G_{\frac{7}{2}}$	$3d^8(^3F)5d\ ^4F_{\frac{7}{2}}$
121,317.732	$3d^8(^3F)5d\ ^4F_{\frac{7}{2}}$	$3d^8(^3F)5d\ ^4G_{\frac{7}{2}}$
121,385.502	$3d^8(^3P)5p\ ^4D_{\frac{3}{2}}$	$3d^8(^3P)5p\ ^4S_{\frac{3}{2}}$
121,456.067	$3d^8(^3P)5p\ ^4S_{\frac{3}{2}}$	$3d^8(^3P)5p\ ^2D_{\frac{3}{2}}$
121,698.855	$^2_{\frac{3}{2}}$	$3d^8(^3F)5d\ ^2D_{\frac{3}{2}}$
121,800.108	$3d^8(^3P)5p\ ^2_{\frac{3}{2}}$	$3d^8(^3P)5p\ ^2P_{\frac{3}{2}}$
122,080.047	$3d^8(^1G)4d\ ^2F_{\frac{5}{2}}$	$3d^8(^3F)5d\ ^4G_{\frac{5}{2}}$
122,144.827	$3d^8(^3F)5d\ ^4G_{\frac{5}{2}}$	$3d^8(^3F)5d\ ^2F_{\frac{5}{2}}$
135,400.429	$3d^8(^3P_2)4f\ [4]_{\frac{7}{2}}$	$3d^8(^3P_2)4f\ [3]_{\frac{7}{2}}$
135,444.263	$3d^8(^3P_2)4f\ [3]_{\frac{7}{2}}$	$3d^8(^3P_2)4f\ [4]_{\frac{7}{2}}$
135,558.601	$^9_{\frac{2}{2}}$	$3d^8(^3P_2)4f\ [5]_{\frac{9}{2}}$
135,849.150	$3d^8(^3P_1)4f\ [3]_{\frac{5}{2}}$	$3d^8(^3P_1)4f\ [2]_{\frac{5}{2}}$
135,879.150	$3d^8(^3P_1)4f\ [3]_{\frac{7}{2}}$	$3d^8(^3P_1)4f\ [4]_{\frac{7}{2}}$
135,953.834	$3d^8(^3P_0)4f\ [3]_{\frac{7}{2}}$	$3d^8(^3P_1)4f\ [3]_{\frac{7}{2}}$
136,122.386	$3d^8(^3P_0)4f\ [3]_{\frac{5}{2}}$	$3d^8(^3P_0)4f\ [3]_{\frac{7}{2}}$
136,290.892	$3d^8(^3P)5d\ ^4D_{\frac{1}{2}}$	$3d^8(^3P)5d\ ^4D_{\frac{3}{2}}$
136,960.448	$3d^8(^3P)5d\ ^4P_{\frac{5}{2}}$	$3d^8(^3P)5d\ ^4F_{\frac{5}{2}}$
137,211.689	$3d^8(^3P)5d\ ^2P_{\frac{1}{2}}$	$3d^8(^3P)5d\ ^2P_{\frac{3}{2}}$

Note.
[a] Energy-level value from this work.

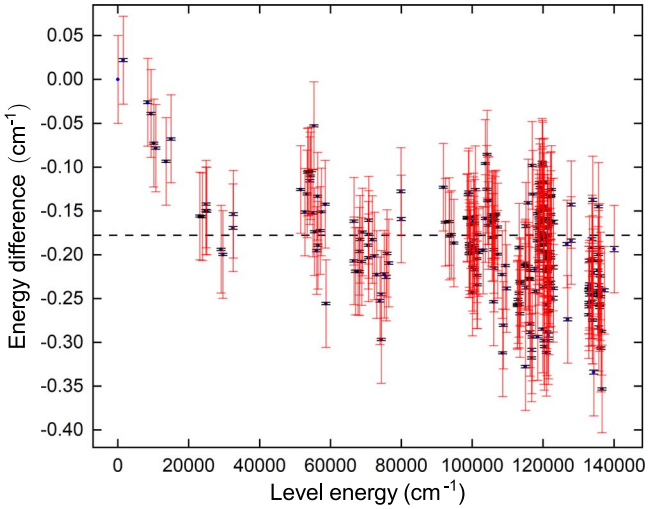

Figure 3. Comparison of the revised Ni II energy levels of this work and previously published values of Sugar & Corliss (1985). The uncertainties of S +C are shown in red and our uncertainties are in black. The dashed line indicates the position of the $-0.17\ cm^{-1}$ shift discussed in Section 2.3.

in a future work may enable missing levels of the $(^3P)5d$ subconfiguration to be found. In total, the 14 new levels of the $(^3P)nl$ subconfigurations allow the new classification of 103 lines for the first time.

6.2.4. New Levels of the $3d^8(^1G)nl$ Subconfigurations

With the identification and optimization of three new levels, $^2F_{\frac{5}{2}}$, $^2D_{\frac{5}{2}}$, and $^2D_{\frac{3}{2}}$, the $(^1G)4d$ subconfiguration is now complete. This has resulted in 28 lines being classified for the first time as transitions between these new levels and other revised levels.

7. Summary

The spectrum of Ni II emitted from Ni–He hollow cathode lamps has been observed from the IR to the VUV, using high-resolution FT spectrometry. Following an extensive term analysis of the spectra, 283 previously reported energy levels of Ni II have been significantly improved in accuracy, with a reduction in energy uncertainty of at least an order of magnitude. A systematic shift in previously published energy levels has also been discovered and corrected for. Twenty-five energy levels with transitions in the IR have also been found and are reported for the first time. This work has produced the most accurate Ni II linelist and energy-level values available to date and will enable more accurate and reliable analyses of Ni II spectral lines in astrophysical spectra.

C.P.C. and J.C.P. thank the STFC of the UK for their support. G.N. was partly supported by NASA award NNH17AE081.

ORCID iDs

Christian P. Clear https://orcid.org/0000-0002-3339-7097
Juliet C. Pickering https://orcid.org/0000-0003-2879-4140
Gillian Nave https://orcid.org/0000-0002-1718-9650
Peter Uylings https://orcid.org/0000-0001-6876-2472

References

Azarov, V. I. 2018, ADNDT, 119, 193
Berglund, M., & Wieser, M. E. 2011, Pure Appl. Chem., 83, 397
Boisse, P., & Bergeron, J. 2019, A&A, 622, A140
Brault, J. W., & Litzén, U. 1983, PhyS, 28, 475
Clear, C. 2018, PhD thesis, Imperial College London
Cowan, R. 1981, The Theory of Atomic Structure and Spectra (Berkeley, CA: Univ. of California Press)
Danzmann, K., Günther, M., Fischer, J., Kock, M., & Kühne, M. 1988, ApOpt, 27, 4947
Delgado Inglada, G., Mesa-Delgado, A., García-Rojas, J., Rodríguez, M., & Esteban, C. 2016, MNRAS, 456, 3855
Dhawan, S., Flörs, A., Leibundgut, B., et al. 2018, A&A, 619, A102
Froese Fischer, C., Godefroid, M., Brage, T., Jönsson, P., & Gaigalas, G. 2016, JPhB, 49, 182004
Haris, K., & Kramida, A. 2017, ApJS, 233, 16
Hartman, H., Nilsson, H., Engström, L., & Lundberg, H. 2015, A&A, 584, A24
Holmes, C. E. 2015, PhD thesis, Imperial College London
Jönsson, P., Gaigalas, G., Rynkun, P., et al. 2017, Atoms, 5, 16
Kirby, E. N., Xie, J. L., Guo, R., Kovalev, M., & Bergemann, M. 2018, ApJS, 237, 18
Kramida, A., Ralchenko, Yu., Reader, J. & NIST ASD Team 2021, NIST Atomic Spectra Database v5.9 (Gaithersburg, MD: National Institute of Standards and Technology) https://physics.nist.gov/asd
Kramida, A. E. 2011, CoPhC, 182, 419
Learner, R. C. M., & Thorne, A. P. 1988, JOSAB, 5, 2045
Liggins, F. S., Pickering, J. C., Nave, G., Ward, J. W., & Tchang-Brillet, W. L. 2021, ApJS, 252, 10
Litzén, U., Brault, J. W., & Thorne, A. P. 1993, PhyS, 47, 628
Nave, G., Griesmann, U., Brault, J. W., & Abrams, M. C. 2015, Xgremlin: Interferograms and spectra from Fourier transform spectrometers analysis, Astrophysics Source Code Library, ascl:1511.004
Nave, G., & Johansson, S. 2013, ApJS, 204, 1
Nave, G., & Sansonetti, C. J. 2004, JOSAB, 21, 442
NSO 2021, NSO Historical Archive: McMath-Pierce Facility, https://nispdata.nso.edu/ftp/FTS_cdrom/
Peck, E. R., & Reeder, K. 1972, JOSA, 62, 958
Pickering, J. C., Teresa Belmonte, M., Clear, C. P., Liggins, F., & Concepcion-Mairey, F. 2020, in IAU Symp. 350, Laboratory Astrophysics: From Observations to Interpretation, ed. F. Salama & H. Linnartz (Cambridge: Cambridge Univ. Press), 220
Radziemski, L. J., & Andrew, K. L. 1965, JOSA, 55, 474
Richardson, N. D., Gies, D. R., & Williams, S. J. 2011, AJ, 142, 201
Sansonetti, C. J., & Nave, G. 2014, APJS, 213, 28
Scott, P., Asplund, M., Grevesse, N., Bergemann, M., & Sauval, a. J. 2015, A&A, 573, A26
Shenstone, A. 1970, JRNBA, 74A, 801
Shenstone, A. 1971, JRNBA, 75A, 335
Sugar, J., & Corliss, C. 1985, Atomic Energy Levels of the Iron-period Elements: Potassium through Nickel (Washington, DC: American Chemical Society)
Thorne, A. P., Harris, C. J., Wynne-Jones, I., Learner, R. C. M., & Cox, G. 1987, JPhE, 20, 54
Thorne, A. P., Pickering, J. C., & Semeniuk, J. 2013, ApJS, 207, 13
Uylings, P. 2021, Complex Atoms described by orthogonal operators, Zenodo, https://doi.org/10.5281/zenodo.5710086
Uylings, P., & Raassen, T. 2019, Atoms, 7, 102
Whaling, W., Anderson, W., Carle, M., Brault, J., & Zarem, H. 1995, JQSRT, 53, 1